Chapter 2

ESTABLISHING THE LIMITS OF DEPLOYABLE REFLECTORS

Article: Scaling Laws for Deployable Mesh Reflector Antennas

This chapter also includes both published work from the following proceedings and new, unpublished sections:

S. P. Dassanayake, J. Suh, M. Thomson, and S. Pellegrino, "Mass, Volume and Natural Frequency Scaling of Deployable Mesh Reflectors," in *AIAA SCITECH 2024 Forum*, 2024, p. 2041. DOI: 10.2514/6.2024-2041.

2.1 Motivation

Consider the structural architecture of the state-of-the-art deployable mesh reflector, AstroMesh illustrated in Fig. 2.1. It is composed of three primary components: two cable nets, a metallic wire mesh, and a deployable perimeter truss. The metallic mesh is attached to the back side of the front cable net, providing a radio-frequency reflective surface that approximates a paraboloid. The accuracy of this approximation depends on the size of the triangular facets, which is determined by the length of the cable elements and the density of nodes on the paraboloid. Both the front and rear cable nets are identical, equally prestressed, and attached to the perimeter truss. Tension ties connecting corresponding node pairs between the front and rear nets provide the normal forces required to achieve the desired paraboloid shape.

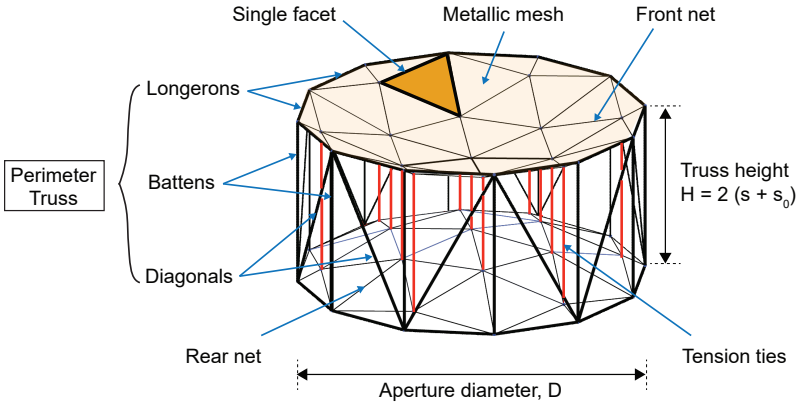

Figure 2.1: Generalized design terminology: structural architecture of faceted deployable mesh reflector.

The deployable perimeter truss consists of identical repeating parallelogram units, each formed by two longerons (i.e., horizontal struts in Fig. 2.1), two battens (i.e., vertical struts in Fig. 2.1), and a diagonal brace that allows for extension when the truss is folded. The truss operates as a cable-actuated, synchronized parallelogram. When stowed, it forms a compact, hollow cylinder, with members secured and preloaded against lightweight hoops that provide stability and debris-protection. This design allows the truss to gently expand upon the release of tie-downs during deployment [40]. The deployed and prestressed structure achieves high stiffness and thermal stability by using high-modulus tubes with a near-zero coefficient of thermal expansion (CTE) for the truss, and thermally stable high-modulus tapes for the cable nets. The reflective surface is made of triangular facets sized according to the operational RF of the reflector. The facet size is chosen

to achieve the required approximation to the paraboloid, quantified by the surface root-mean-square (RMS) error, δ_{RMS}.

As described in Section 1.3, the key metrics for evaluating deployable mesh reflectors include mass and stowed volume (important for launch accommodation), and natural frequency of vibration (related to dynamic performance during operation), which become increasingly significant as the reflector size increases. Despite the importance of mass and stowed volume for large deployable mesh reflectors, systematic studies are lacking, with most research focusing on RF efficiency. Existing studies on dynamics are limited, as high-fidelity models lack computational efficiency.

Given these challenges, this chapter focuses on developing simplified analysis methods that allow for quick estimation of key parameters for deployable reflectors. This approach is not intended to replace more detailed design methods that have been presented elsewhere but serves as a foundation for scaling studies. It extends existing data for deployable mesh reflectors, offering a basis for comparison with reflectors designed for ISA. A general design framework is established for faceted mesh reflector antennas, utilizing a simplified geometric approximation to estimate the maximum facet size and a fundamental approach for designing the facet geometry.

The study then addresses the required connectivity between the edges of the faceted surface and the deployable perimeter truss to ensure that the front cable net can be uniquely prestressed (i.e., to form a statically determinate structure) and maintain a unique (i.e., a kinematically determinate) shape. Once the structure's geometry is determined, the prestress distribution is optimized by adjusting the tension in the ties, and the structural components are sized to provide sufficient safety margins against relevant failure modes.

This design methodology is applied to create deployable center-fed mesh reflectors with an operational frequency of 10 GHz and apertures up to 200 meters in diameter. Scaling laws for mass, stowed volume, and natural vibration frequency are derived, considering various boundary conditions that determine the behavior of reflectors on spacecraft with inertia that is either comparable or much smaller than the reflector. A semi-analytical model is used to significantly reduce computational complexity of numerical analysis compared to fully detailed models.

2.2 Geometry, Connectivity, and Prestress

2.2.1 Geometry and Design for Kinematic and Static Determinacy

A paraboloidal reflective surface is used for maximizing antenna directivity [56]. Figure 2.2 illustrates a circular paraboloid defined by its axis z, aperture diameter D, focal length F, and z-offset s_0. The equation for the surface is:

$$s_0 + \frac{(x^2 + y^2)}{4F^2} = z \tag{2.1}$$

which depends on the key geometric parameter, the F/D ratio, with higher values corresponding to shallower reflectors. This study considers reflector designs with three different values, $F/D = 0.5, 0.7$, and 1.0.

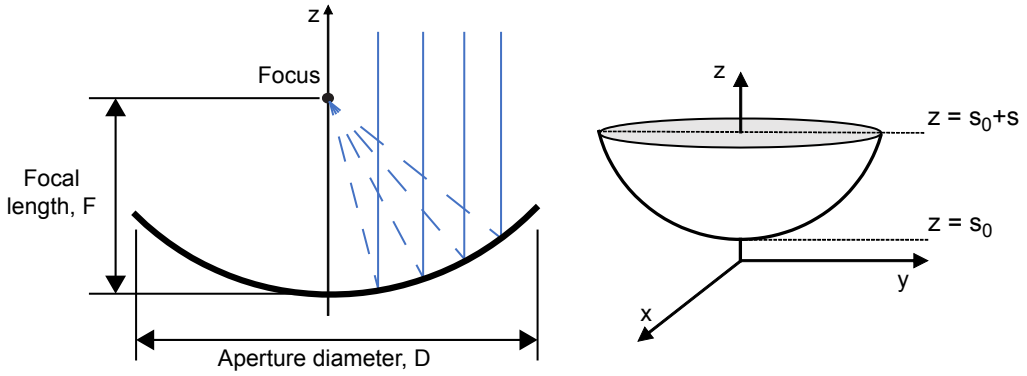

Figure 2.2: Geometry of paraboloidal reflector.

For designing a faceted surface, it is convenient to approximate the paraboloid with a surface of uniform curvature, a sphere. The spherical cap that aligns with the apex and edge of the paraboloid has a radius R as described in [57] and is given by:

$$R = 2F + \frac{D^2}{32F}. \tag{2.2}$$

The required size of the triangles for smooth approximation of the reflector surface is then estimated by analyzing the geometric deviation between a spherical surface of radius R and an equilateral triangle of side length L, whose vertices lie on the curved surface. This RMS error of the facet, described in [58] is given by:

$$\delta_{facet} = \frac{L^2}{8\sqrt{15}R} \tag{2.3}$$

and is used to calculate the appropriate facet size for a given R and F/D.

When a tessellation of equilateral triangles of side length L in the $x-y$ plane is vertically projected onto a paraboloid, the facets increasingly elongate as they move away from the z-axis. However, this elongation is minimal for relatively flat reflectors and small L/D ratios.

In this study, geometric faceting is considered the only source of error, neglecting other potential error sources, such as thermal distortions, spillover, aperture taper, cross polarization, etc. The RMS surface error is therefore set equal to the faceting error in Eq. 2.3, i.e., $\delta_{RMS} = \delta_{facet}$. For a reflector operating at 10 GHz, with an error limit of $\lambda/50 = 0.6$ mm, the maximum allowable facet size is calculated using Eqs. 2.2 and 2.3. It is important to note that the lengths in Eq. 2.3 are not the unstressed lengths of the cable net elements, but account for the elastic stretching caused by prestress.

Figure 2.3(a) shows how the facet size varies with different F/D ratios. Larger facets are feasible for higher F/D values as they correspond to shallower reflectors for the same aperture size. As a general rule, the maximum facet size increases proportionally to $\sqrt{D}$. Figure 2.3(b) shows the net configuration, where, after selecting a facet size for the given aperture and F/D, the number of subdivisions n in the hexagonal tessellation is calculated using the relationship:

$$n = 0.5D/L. \tag{2.4}$$

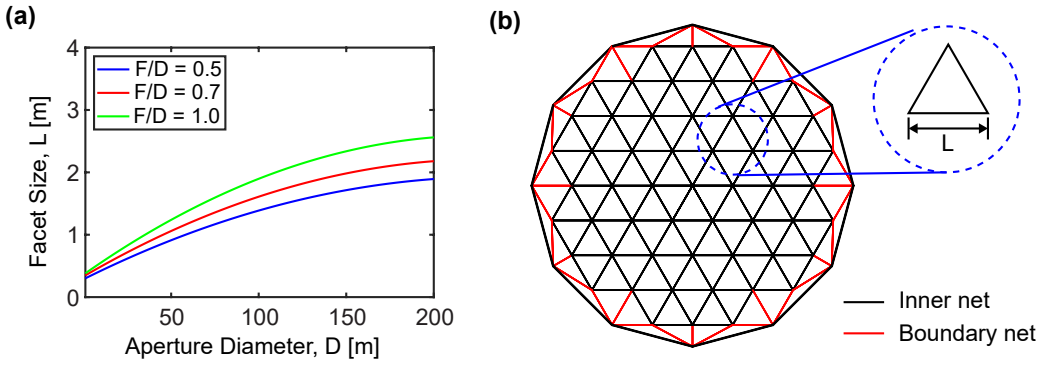

Figure 2.3: Faceting of paraboloidal surface: a) variation of facet size with diameter and b) schematic layout of net.

The front and rear reflector nets consist of *inner net* cables forming the regular hexagonal tessellation, indicated by black solid lines in Fig. 2.3(b) and *boundary net* cables connecting the triangles to the perimeter truss, indicated by red solid lines in Fig. 2.3(b). The inner net consists of *free nodes* connected by tension ties between

the front and rear nets. Although the inner net geometry is unique for a given facet size, the boundary net design can vary based on the number of bays in the perimeter truss and the number of connection points between the perimeter truss and the inner net. Figure 2.4 presents three different boundary net designs with identical number of edge subdivisions ($n = 7$), but varying connections between perimeter truss nodes and free nodes. It is important to note that in the design of the boundary cables, it is assumed that each node of the perimeter truss is connected to an equal number of free nodes, denoted as n_c. The number of subdivisions in one-sixth of the perimeter truss is denoted by n_t. A similar approach was previously adopted in [59].

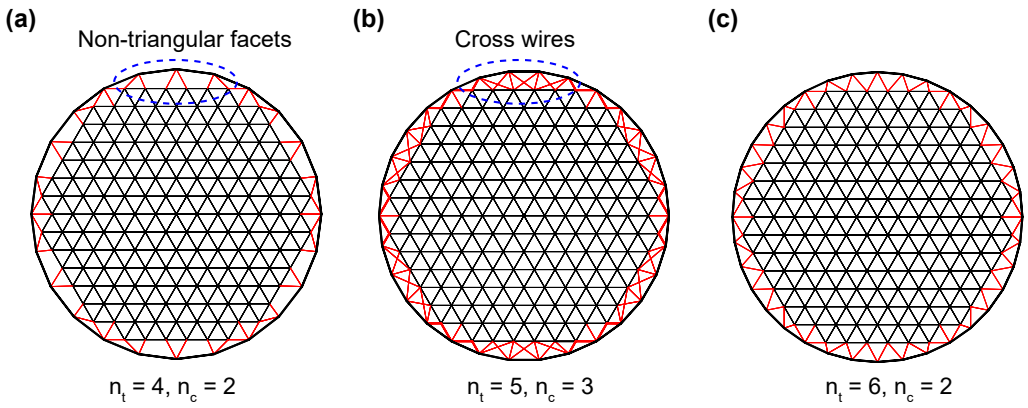

Figure 2.4: Three different net configurations with a) non-triangular facets, b) cross wires, and c) complete triangular tessellation.

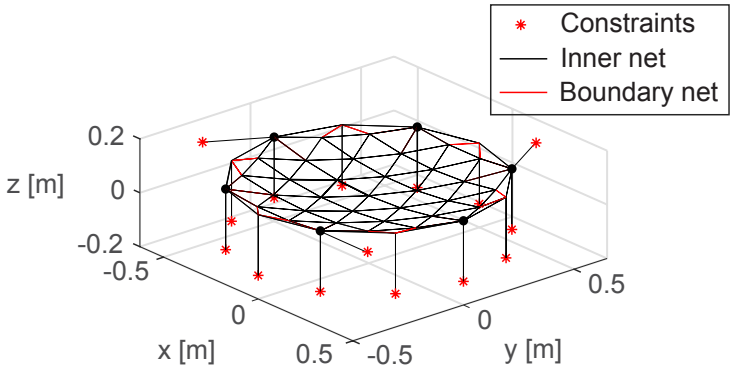

Figure 2.5: Pin-jointed bar model of front net for $n = 3, n_t = 2, n_c = 2$.

To ensure that the reflector has a unique shape and prestress distribution, the degrees of kinematic and static determinacy are analyzed using the pin-jointed bar model of each cable net, as depicted in Fig. 2.5. This analysis, based on Maxwell's

extended equation and equilibrium matrix rank [4], [60], [61], shows that these properties depend on the net geometry. For example, non-triangular facets (Fig. 2.4(a)) result in a kinematically indeterminate structure, while cross-wired boundary nets (Fig. 2.4(b)) lead to static indeterminacy. Only configurations with triangular facets and no cross-wires (Fig. 2.4(c)) are both kinematically and statically determinate, making them the preferred choice for the structural architecture of the reflector.

For reflectors designed in this manner, the number of subdivisions of the hexagonal tessellation is related to the number of free nodes connected to each node of the perimeter truss and the subdivision of the perimeter truss by the relationship:

$$n - 2 = (n_t - 1)\,(n_c - 1)\,. \tag{2.5}$$

In this study, the perimeter truss is designed to have half the density of the net, with each batten supporting three free nodes through boundary cables (i.e., $n_c = 3$ in Eq. (2.5)). The lengths of the truss members; longerons, battens, and diagonals, are determined based on the designed net geometry.

2.2.2 Prestress Optimization of Cable Nets

Optimizing the prestress of the reflector is crucial since the prestress directly impacts the structural mass. A higher prestress leads to increased loading on the structural elements, which in turn requires them to be larger and therefore heavier. This effect is particularly pronounced in the elements of the perimeter truss that experience compression due to prestress. It will be demonstrated that, for large-diameter reflectors, designs utilizing optimal prestress are substantially lighter compared to those with non-optimized prestress.

Given the structure's statically determinate design, the prestress distribution is uniquely defined by the equilibrium equations for the nodes once the tension tie forces are applied. For example, the equilibrium equation in the x-direction for each free node, i, connected to N nodes, j, is (see [4] for more details) given by:

$$\sum_{j}^{N} \frac{x_i - x_j}{L_{ij}} p_{ij} = t_{i,x} \tag{2.6}$$

where,
L_{ij} is the length of cable ij, and hence $L_{ij} = \sqrt{\left(x_i - x_j\right)^2 + \left(y_i - y_j\right)^2 + \left(z_i - z_j\right)^2}$;
p_{ij} is the tension in cable ij;
$t_{i,x}$ is the component of the tension tie force applied to node i, in the x-direction.

The simplest approach involves computing the prestress for a single tension tie force value at all free nodes. However, this method results in several cables near the transition between the inner and boundary nets being under compression (and in practice, slack). To achieve a purely tensile prestress distribution, the tie forces at the free nodes in the transition region must be increased by a suitable factor, $\alpha > 1$, from their nominal value.

Figure 2.6(a) illustrates the prestress distribution in the cable net for $D = 200$ m, $F/D = 1.0$, and $\alpha = 1.7$. This value was determined through trial and error. This approach of applying two distinct tie forces led to a reduction in overall structural mass, suggesting that further mass reduction could be achieved through a more formal optimization of general prestress distributions.

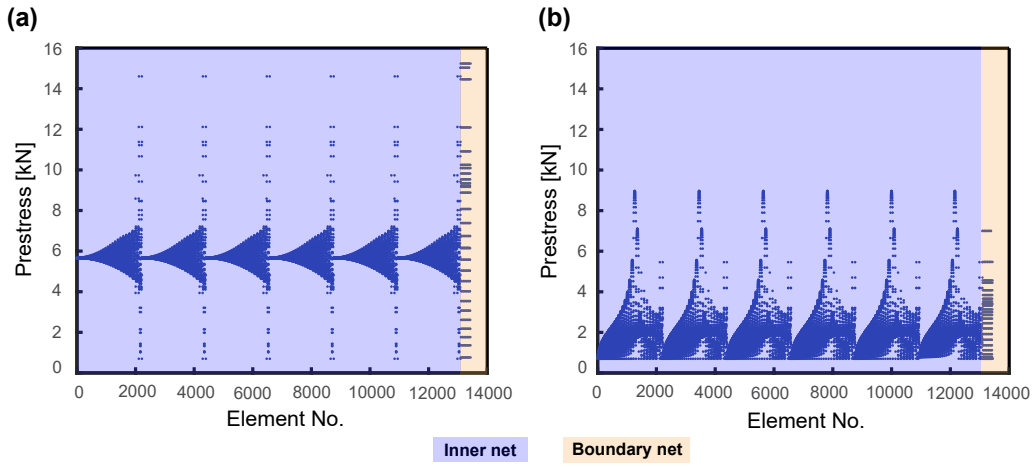

Figure 2.6: Comparison of cable prestress distributions for $D = 200$ m, $F/D = 1.0$ corresponding to (a) 2 distinct tension tie forces, and (b) $(n + 1)$ rings of tension tie forces.

Theoretically, varying the tie forces at each free node could be explored, but this is impractical. To simplify practical implementation, six-fold rotational symmetry of the hexagonal tessellation was assumed. Therefore, the number of distinct tension tie forces was set to the number of *rings* (see Fig. 2.7) in the tessellation, i.e., $n+1$. This approach can be extended to offset reflectors, for which the assumption of six-fold symmetry is not valid, by considering larger sets of cable tensions for each ring of tension tie forces.

A basis for independent tension tie forces, T, was considered by computing the distribution T^k that corresponds to unit tension tie forces at all free nodes on ring k and zero forces at all other free nodes. Denoting the resulting prestress distribution

in equilibrium with T^k as P^k, the following two matrices were defined:

$$T = \left[\underline{T}^1 \ \underline{T}^2 \ \cdots \ \underline{T}^{n+1}\right] \tag{2.7a}$$

$$P = \left[\underline{P}^1 \ \underline{P}^2 \ \cdots \ \underline{P}^{n+1}\right]. \tag{2.7b}$$

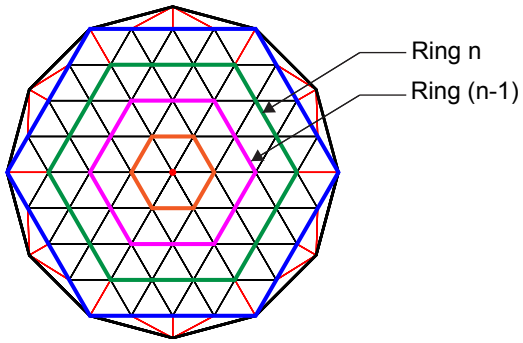

Figure 2.7: Definition of *rings* in inner net.

A general tie force distribution is $T\alpha$, with corresponding cable tensions p_{ij} given by $P\alpha$, where the coefficients $\alpha_k > 0$ to ensure that all tension tie forces are positive.

An additional constraint is that a sufficient level of pretension must be applied to all cables to keep them both under tension and sufficiently straight when loaded by the prestressed metallic mesh. The minimum required tension is [62]:

$$p_{ij} \geq 10\sigma L_{max} \tag{2.8}$$

where,
σ is the biaxial prestress in the metallic mesh;
L_{max} is the maximum cable length in the net.

Different objective functions were evaluated for optimization using MATLAB's *fmincon* function, focusing on two metrics: the maximum compressive forces in the perimeter truss and the range of cable tensions, $\frac{(P)_{max}}{(P)_{min}}$. Both metrics contribute directly to the overall structural mass, as discussed in Sections 2.3 and 2.4. The results, presented in Table 2.1, show that all variants considered improve both metrics. Remarkably, five out of seven different objective functions resulted in a 32% reduction in mass and a 41% reduction in the range of cable tensions. Among these, the average batten force in the perimeter truss was chosen as the objective function for prestress optimization.

Visual comparison of the cable force distribution for the initial two-tension tie force solution, Fig. 2.6(a), with the optimal distribution obtained in this manner, Fig. 2.6(b), for $\sigma = 5$ N/m is interesting. It reveals that the optimal solution results in significantly lower cable tensions.

Table 2.1: Comparison of Objective Functions for $D = 200$ m, $F/D = 1.0$

Objective Function	$\frac{P_{max}}{P_{min}}$	Maximum Compressive Force (kN)	Mass (kg)
RMS Deviation of cable tensions	10.546	145.25	13,259
Range of cable tensions	10.027	138.71	13,039
Maximum longeron force	12.816	138.42	13,030
Average longeron force	12.816	138.42	13,030
Maximum batten force	12.816	138.42	13,030
Average batten force	12.816	138.42	13,030
Sum of tension tie forces	12.816	138.42	13,030
Solution with two distinct tension tie forces	21.775	379.47	19,061

2.2.3 Potential Modifications to the Minimum Tension Requirement

In Eq. 2.8, the minimum tension requirement for the cable elements is governed by the maximum cable length in the net, L_{max}, for a given σ. Examining the original net configuration for $D = 100$ m in Fig. 2.8(a) reveals that L_{max} is predominantly determined by the boundary cable elements, regardless of the subdivision n of the central hexagon.

One possible modification to address this issue is to shift the outermost rings of the central hexagon outward (see [63] for similar approaches). This was attempted, as shown in Fig. 2.8(b), by positioning the centers of the two outermost ($n + 1$ and n) cable rings at one-third of the maximum radial distance between the $n - 1^{th}$ ring and the perimeter truss, while distributing the remaining nodes equally in the radial direction. Mapping the tessellation in this manner preserves the original configuration of the perimeter truss, along with its static and kinematic determinacy, while maintaining the surface accuracy dictated by the subdivision n in the central hexagon. At the same time, it enhances the surface accuracy in the boundary net. However, if all cable net rings are shifted outward, as shown in Fig. 2.8(c), the surface accuracy at the center is compromised, and the fabrication of the cable net becomes more complex due to the lack of straight cable elements running across the entire diameter, unlike the nets in Figs. 2.8(a) and (b).

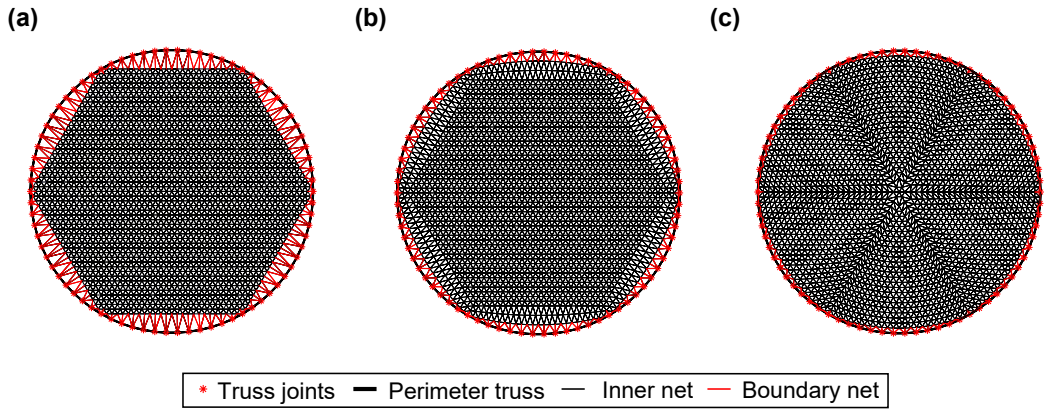

Figure 2.8: Cable net configuration for $D = 100$ m, $n_t = 13, n_c = 3$: a) original configuration, b) mapped configuration 1, and c) mapped configuration 2.

Table 2.2 presents the optimization results for the prestress distributions, comparing the original cable net configuration with the mapped version shown in Fig. 2.8(b). The objective function used for this comparison is the average batten force, as chosen in Section 2.2.2. The results demonstrate that reducing L_{max}, and consequently lowering the minimum tension requirement, leads to a substantial reduction in key metrics of interest, including structural mass. Although this mapping approach offers no advantages for smaller apertures, the benefits are significant for larger apertures, as shown in the results for $D = 200$ m.

Table 2.2: Comparison of cable net configurations for $D = 100, 200$ m, $F/D = 1.0$

Cable net configuration	Radius of Longeron (mm)	$\frac{P_{max}}{P_{min}}$	Maximum Compressive Force (kN)	Mass (kg)
$D = 10$ m				
Original	6.145	3.308	1.07	22.5
Mapped	6.297	4.338	1.15	22.9
$D = 100$ m				
Original	45.434	6.060	29.18	2,479
Mapped	38.956	6.598	18.40	2,184
$D = 200$ m				
Original	94.102	12.816	138.42	13,030
Mapped	68.742	10.060	53.96	9,815

However, the original cable net configuration was chosen for the rest of the analysis presented in this thesis due to its much simpler fabrication of the inner net using only straight cable elements, compared to the complex mapped version.

2.3 Structural Design

2.3.1 Metallic Mesh and Cable Net Design

For the reflector design, a knitted gold-plated molybdenum wire mesh with an areal density $\rho_{mesh} = 0.025$ kg/m^2 was chosen, with a biaxial prestress $\sigma =$ 5 N/m. The front and rear nets are composed of thin CFRP (carbon fiber reinforced polymer) strips made from M55J carbon fiber in a thermoplastic matrix [64]. This composite material has a density $\rho_n = 1,786$ kg/m^3 and a longitudinal modulus $E_n = 325.4$ GPa. A rectangular cross section of 6 mm width and 150 μm thickness was selected for all reflector apertures. The smallest separation between the front and rear nets (denoted $2s_0$) was kept constant at 0.1 m across all reflector designs considered in this study, as larger separations would increase the batten lengths. The pretension in the cable nets was derived from the optimization process described in Section 2.2.2. Using the net prestress, the resulting compression forces in the perimeter truss were determined through the equilibrium equations of the truss joints. The prestress analysis results for reflectors with apertures $D = 10$ m, 100 m, and 200 m are presented in Table 2.3.

Table 2.3: Prestress range (Nets: tension; Truss: compression), for $F/D = 1.0$

	Nets (kN)		Truss (kN)	
D(m)	Inner net	Boundary net	Longerons	Battens
10	0.042 ~ 0.114	0.045 ~ 0.139	0.947 ~ 1.072	0.046 ~ 0.052
100	0.357 ~ 2.160	0.357 ~ 1.838	25.794 ~ 29.182	0.484 ~ 0.567
200	0.700 ~ 8.967	0.700 ~ 7.000	120.220 ~ 138.420	1.545 ~ 1.859

2.3.2 Perimeter Truss Design

Due to the significant compressive forces acting on the perimeter truss, tubes with circular cross sections were selected for all structural members. A minimum diameter of 5 mm was chosen to avoid impractically small tube sizes.

Assuming pin-ended conditions, the global critical buckling load, P_{cr}, for a thin-walled circular tube with length l, cross-sectional radius r, and thickness t is given by:

$$P_{cr} = \frac{\pi^3 r^3 t E}{l^2} \tag{2.9}$$

where E is the longitudinal modulus.

The longerons, which experience the highest compressive forces, were sized first. Their thickness was set to 1.0 mm, and the radius was calculated using Eq. 2.9,

with a safety margin of 2. The battens and diagonals were then designed with the same cross-sectional radius as the longerons to simplify and lighten the joints of the perimeter truss. The minimum thickness for the battens was set at 1.25 mm, and it was confirmed that the buckling load from Eq. 2.9 exceeded the compressive forces acting on them.

Although the diagonals theoretically do not experience compression, they are loaded in bending during deployment. Thus, their size was simply set to match the longerons, but with a thickness of 0.75 mm.

The radius and thickness values for the longerons, battens, and diagonals for reflectors with apertures D = 10 m, 100 m, 200 m are presented in Table 2.4.

Table 2.4: Size of perimeter truss members, for $F/D = 1.0$

D(m)	Radius of Longeron/ Batten/Diagonal (mm)	Thickness of Longeron (mm)	Thickness of Batten (mm)	Thickness of Diagonal (mm)
10	6.15	1.00	1.25	0.75
100	45.43	1.00	1.25	0.75
200	94.10	1.00	1.25	0.75

2.3.3 Joint Design

The mass of the perimeter truss joints was estimated for a general aperture D and varying values of F/D using a parametric design process based purely on geometry. The structure consists of two types of joints: Type-1, which connects five structural elements (longeron, diagonal, batten, diagonal, and longeron), and Type-2, which connects three structural elements (longeron, batten, and longeron), as illustrated in Fig. 2.9(a).

The general configuration of both joint types is depicted in Figs. 2.9 and 2.10. The design features two parallel plates made of CFRP (with the same material properties as the struts and cable net elements) connected centrally to a plate made of 6061 aluminum alloy (ρ_{Al} = 2700 kg/m^3, E_{Al} = 69 GPa). This central plate is securely fastened to the batten, while the longerons and diagonals are attached to appropriate locations on the side plates via 6061 aluminum alloy sleeves and steel pins and bolts (ρ_S = 7800 kg/m^3, E_S = 210 GPa). These connections allow rotational movement, facilitating stowage and deployment.

Once the diameter of the longerons was determined, as discussed in Section 2.3.2, the positions of the pins attaching the longerons and diagonals to the plates were

meticulously planned to ensure adequate clearance, allowing the members to rotate freely around the pins. Note that the battens are rigidly connected to the joints. The thicknesses of the plates and sleeves were selected based on allowable margins for hole bearing failure at the pin attachments (~thickness ≥ 3× hole diameter [65]).

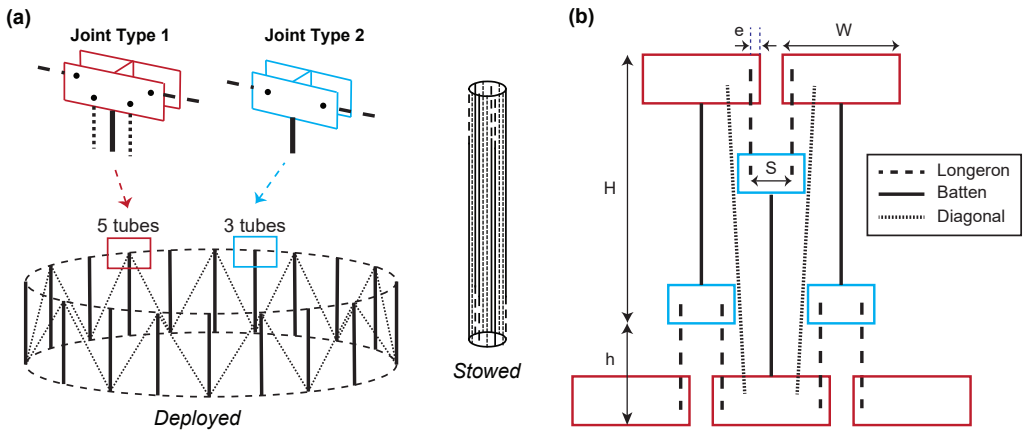

Figure 2.9: Perimeter truss: a) fully deployed and stowed configurations, and b) relative position of members in stowed configuration.

Both joints were designed with the CAD software SolidWorks and the mass of each joint type was obtained from SolidWorks. Figure 2.10 shows the Type-1 and Type-2 joints and the end sleeves that stiffen the tubular elements.

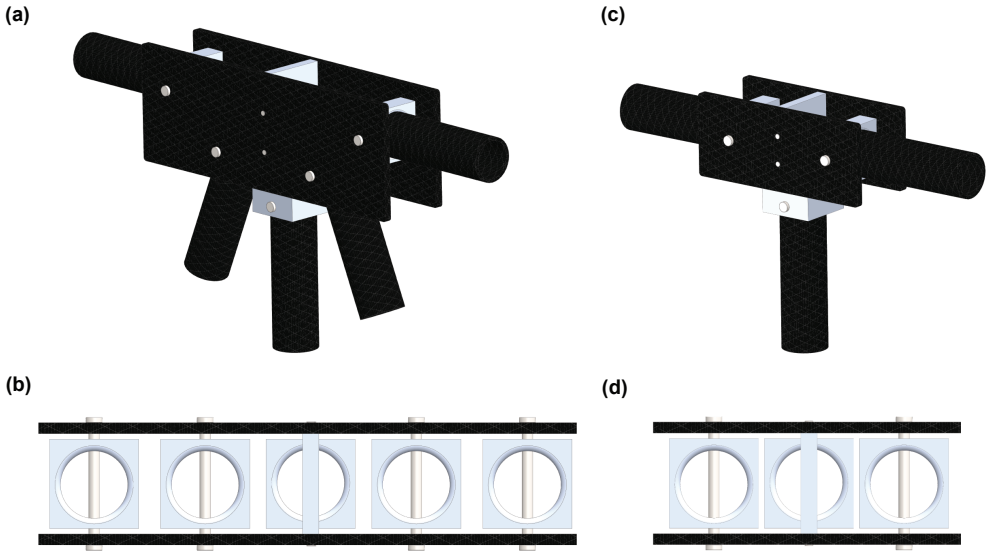

Figure 2.10: CAD images of a) Type-1 joint with 5 struts, b) Type-1 joint strut sleeves, c) Type-2 joint with 3 struts, and d) Type-2 joint strut sleeves.

The mass of the joints for apertures of D = 1 m, 10 m, 100 m, and 200 m, and F/D = 1.0, is presented in Table 2.5.

Table 2.5: Joint masses for F/D = 1.0

	Joint Mass (g)	
D(m)	Type-1	Type-2
1	18.0	10.3
10	45.2	23.2
100	2, 272	1, 076
200	10, 780	5, 284

2.4 Scaling of Mass and Volume

2.4.1 Estimating Mass and Stowed Volume

The total mass of the reflector was estimated by summing the contributions from the cable nets (m_n), metallic mesh (m_{mesh}), perimeter truss (m_{truss}), tension ties (m_{tt}), joints (m_j), and deployment actuators (m_{dep}):

$$m_{total} = m_n + m_{mesh} + m_{truss} + m_{tt} + m_j + m_{dep}. \tag{2.10}$$

The mass of each component was calculated based on the structural design described in Section 2.3. The mass of the cable net was determined from the cross-sectional area of the strips, multiplied by their total length and material density. The metallic mesh mass was calculated assuming full coverage of the front net's surface, where the area of the paraboloid was multiplied by the mesh's areal density. The perimeter truss mass was derived from the design of the longeron, batten, and diagonal members, as detailed in Section 2.3.2. The mass of the joints was estimated by linear interpolation of the values in Table 2.5. For the tension ties and seams in the mesh, m_{tt}, it was assumed to be twice the mass of the metallic mesh ($2\times m_{mesh}$). The mass of the deployment actuators was assumed to be 10% of the total reflector mass.

The stowed envelope of the reflector was assumed to be of cylindrical shape, as illustrated in Fig. 2.9(a). The diameter of this cylinder is determined by the perimeter of the stowed configuration, where adjacent joints are in contact. The height of the cylinder is defined by the lengths of the battens and longerons. Figure 2.9(b) presents a schematic showing the relative positions of the truss members at the joints and the design parameters influencing the stowed dimensions. In Fig. 2.9(b), H represents the total height of the fully deployed perimeter truss, while h defines the distance between the bottom edges of the Type-1 and Type-2 joints in the folded

configuration. The length of a Type-1 joint, the distance between the center of the hinge of the longeron and the edge of the joint, and the distance between the centers of the hinges of the longerons in a Type-2 joint are defined as W, e, and S, respectively. The perimeter of the stowed reflector P_{stowed} is then calculated as:

$$P_{stowed} = (W + S - 2e) \times (3n_t) \tag{2.11}$$

and then the diameter in the stowed configuration is given by $D_{stowed} = P_{stowed}/\pi$. The height of the stowed configuration is $H_{stowed} = H + h$.

2.4.2 Mass and Stowed Dimensions Results

The variation in the equivalent areal density of different reflector components is plotted in Fig. 2.11 against the aperture size, for $F/D = 1.0$. A comparison of the two graphs highlights the superior mass efficiency achieved with the optimal prestress distribution. For the design with two distinct tension tie forces (Fig. 2.11(a)), the areal density increases nonlinearly as the reflector diameter grows. This is mainly due to the rapidly rising mass of the battens and diagonals in the perimeter truss. In contrast, the design with the optimal prestress distribution, shown in Fig. 2.11(b), results in smaller compressive forces in the perimeter truss compared to the two-tension design. The difference between the two approaches is minimal for apertures below 50 m but, as the diameter increases, the lower prestress in the truss leads to smaller member sizes and nearly a one-third reduction in areal density for apertures around 200 m.

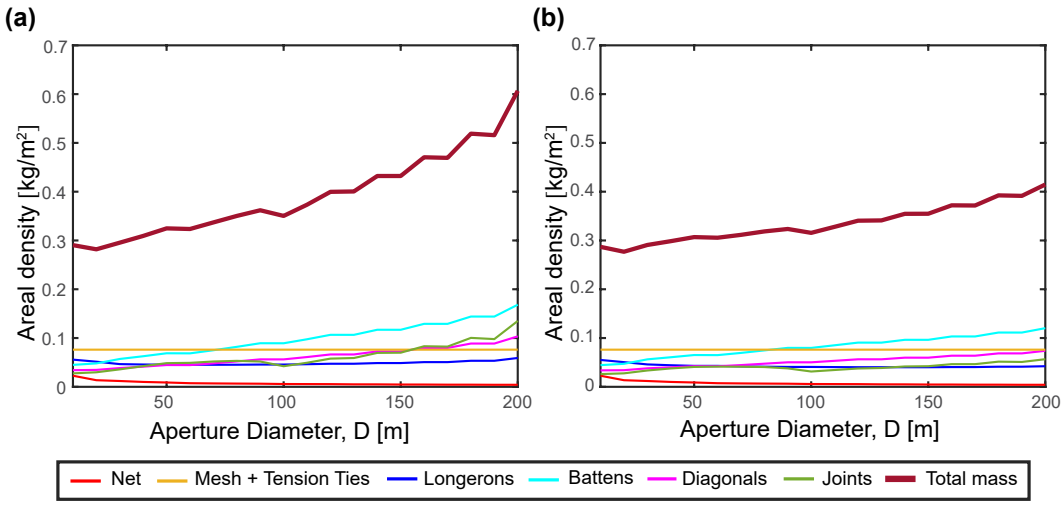

Figure 2.11: Areal density of reflector components ($F/D = 1.0$): a) non-optimal prestress design, and b) optimal prestress design.

Figure 2.12 presents the overall mass, stowed diameter, and height of the reflector for $F/D = 1.0$ across a diameter range of 10 m to 200 m.

Two launch vehicles, Falcon Heavy [66] and Starship [67], were selected to assess the feasibility of launching large-aperture mesh reflectors. In Fig. 2.12(b) and (c), the pink and blue solid lines represent the payload capacity limits for Falcon Heavy and Starship, respectively. According to the respective Users' Guides, the maximum payload mass limits to geostationary transfer orbit (GTO) are 26, 700 kg for the Falcon Heavy and 21, 000 kg for the Starship. Even the largest reflectors considered in this study remain well within these mass limits. However, launch envelope constraints, particularly the stowed diameter, are much stricter. Reflectors with apertures larger than 70 m exceed Falcon Heavy's payload capacity, while 100 m is the maximum aperture limit for launch aboard Starship.

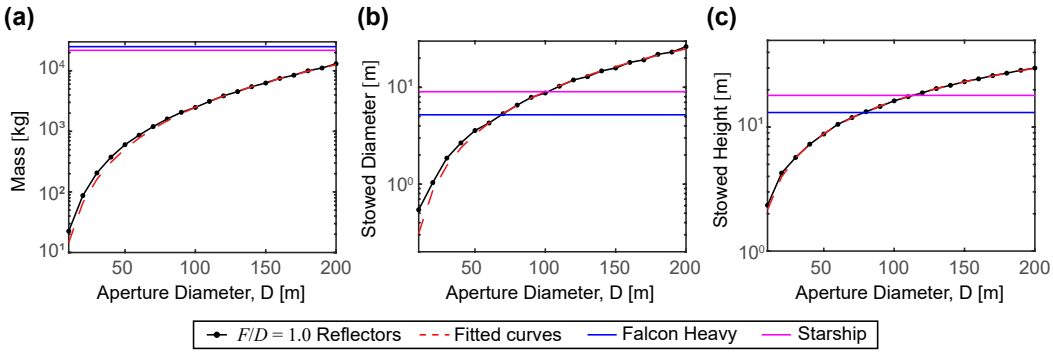

Figure 2.12: Scaling of deployable reflectors for $F/D = 1.0$: a) total mass, b) stowed diameter, and c) stowed height.

This scaling analysis provides valuable insights into the challenges of launching large-scale deployable mesh reflectors, showing that launch feasibility is primarily constrained by the stowed diameter of the reflector, followed by its height. The launch mass limit, in contrast, is not as restrictive. Given that extremely large space-borne deployable reflectors are impractical within current launch vehicle limitations, there is a clear need to explore alternative strategies, such as on-orbit assembly, to overcome these volumetric payload constraints.

2.4.3 Analytical Scaling Laws

The results presented in Section 2.4.2 can be used to establish analytical scaling laws for the mass and stowed envelope of deployable mesh reflectors designed with the optimized prestress distribution described in Section 2.2.2.

To derive a mass scaling equation, the reflector components were categorized into three groups that scale similarly according to the structural design procedure; the mass of the perimeter truss including the joints, the mass of the cable net, and the mass of the mesh and tension ties. Each mass category was expressed as a separate power function of the aperture diameter D, as illustrated in Fig. 2.13. The mass data of each category were fitted to this power law using MATLAB's curve fitting algorithm, ensuring a 95% confidence interval for the results. The coefficients of the power law terms, c_1, c_3 and c_5, were scaled to reflect the mass of the deployment actuators, which was set at 10% of the total mass. The resulting scaling law for the mass (in kg) of reflectors with $F/D = 1.0$ is:

$$m_{total} = 0.022D^{2.452} + 0.054D^{1.492} + 0.067D^2. \tag{2.12}$$

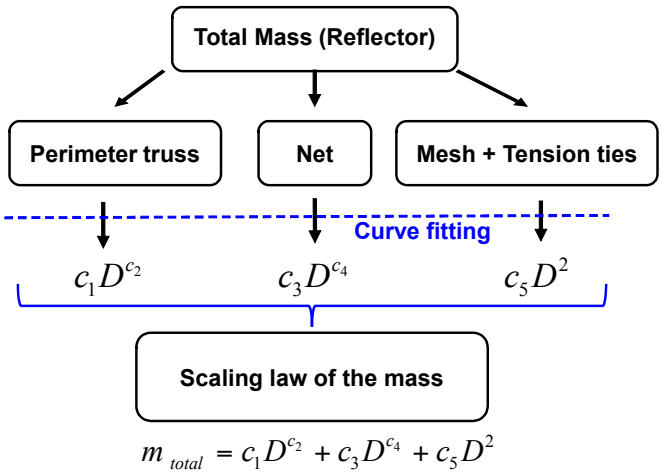

Figure 2.13: Process of establishing a scaling law for the total mass.

The perimeter truss is clearly the largest contributor to the mass, with $c_2 > 2$, followed by the mesh and tension ties, and finally the cable net. Figure 2.12(a) plots the detailed mass of reflectors with $F/D = 1.0$ alongside this analytical expression, demonstrating that Eq. 2.12 closely follows the total mass of the reflector.

When considering the stowed diameter and height of the deployable reflector, the contributions from the cable nets, mesh, and tension ties are negligible, see Fig. 2.9. Instead, the stowed envelope size is primarily influenced by the perimeter truss members and joints. Consequently, single-term power functions were used to derive the following analytical expressions for the diameter and height:

$$D_{stowed} = 0.011D^{1.464} \tag{2.13}$$

$$H_{stowed} = 0.286D^{0.877} \tag{2.14}$$

which have been plotted in Fig. 2.12(b) and (c).

2.4.4 Scaling Studies for Deeper Reflectors

Mass and stowed volume scaling plots for $F/D = 0.5, 0.7$, generated using the same overall design methodology, are presented in Fig. 2.14. The corresponding joint masses for apertures of $D = 1$ m, 10 m, 100 m, and 200 m are listed in Table 2.6. In the plots, black circular dots and red crosses represent the quantities calculated for $F/D = 0.5$ and $F/D = 0.7$ reflectors, respectively.

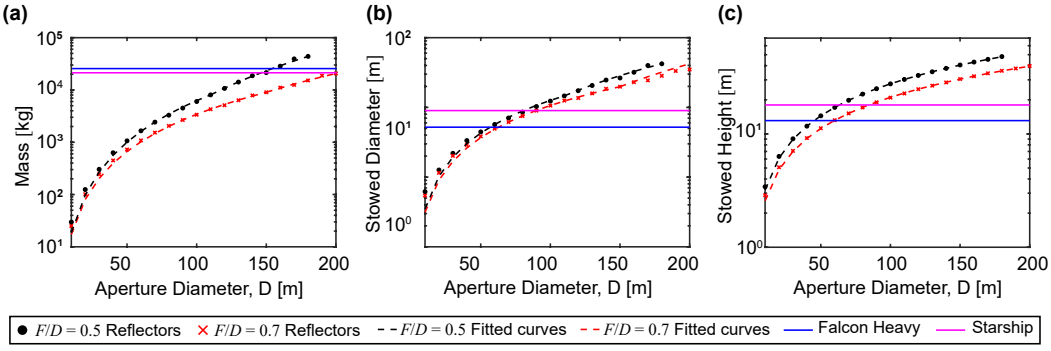

Figure 2.14: Scaling of deployable reflectors for $F/D = 0.5$ and 0.7: a) total mass, b) stowed diameter, and c) stowed height.

Table 2.6: Joint masses for $F/D = 0.5, 0.7$

	Joint Mass (g)			
	$F/D = 0.5$		$F/D = 0.7$	
D(m)	Type-1	Type-2	Type-1	Type-2
1	18.0	10.3	18.0	10.3
10	40.5	21.2	45.2	23.2
100	2,343	1,107	2,217	1,051
200	18,448	9,290	15,381	7,687

These plots show that both the mass and stowed envelope increase as the reflectors become deeper, i.e., as F/D decreases. Reflectors with $F/D = 0.5$ and aperture diameters greater than 140 m are constrained by the payload mass capability of the launchers. As with the $F/D = 1.0$ case, the primary challenge is not the mass,

but the launch envelope restrictions. However, for $F/D = 0.5$ and $F/D = 0.7$, the stowed height becomes the most restrictive factor, as opposed to the stowed diameter, due to the increased depth of the cable nets. For reflectors with $F/D = 0.5$, an aperture diameter of 50 m is the limit for the Falcon Heavy, while the Starship can accommodate up to 60 m. For $F/D = 0.7$, the aperture limit increases to 60 m for the Falcon Heavy and 80 m for the Starship.

Analytical scaling laws for the mass and stowed envelope of reflectors with $F/D = 0.5$ and $F/D = 0.7$ were established using a similar approach to that used for $F/D = 1.0$, which involves grouping reflector components into three distinct categories. However, it was observed that reflectors with $n \geq 32$ exhibit different trends compared to those with $n < 32$. As a result, separate analytical expressions were formulated for each case, and are plotted on Figs. 2.14(a-c). Specifically, for $F/D = 0.5$, reflectors with $D \geq 110$ m have $n \geq 32$, while for $F/D = 0.7$, reflectors with $D \geq 150$ m have $n \geq 32$.

The analytical expressions for the total mass (m_{total}), stowed diameter (D_{stowed}), and stowed height (H_{stowed}) for $F/D = 0.5$ are as follows:

$$
\begin{aligned}
m_{total} &= \begin{cases} 0.014 \times D^{2.767} + 0.064 \times D^{1.5} + 0.063 \times D^2 & (n < 32) \\ 0.003 \times D^{3.572} + 0.064 \times D^{1.5} + 0.063 \times D^2 & (n \geq 32) \end{cases} \\
D_{stowed} &= \begin{cases} 0.0097 \times D^{1.557} & (n < 32) \\ 0.0006 \times D^{2.155} & (n \geq 32) \end{cases} \\
H_{stowed} &= \begin{cases} 0.370 \times D^{0.9368} & (n < 32) \\ 0.363 \times D^{0.9411} & (n \geq 32). \end{cases}
\end{aligned}
\tag{2.15}
$$

The analytical expressions for the total mass (m_{total}), stowed diameter (D_{stowed}), and stowed height (H_{stowed}) for $F/D = 0.7$ are as follows:

$$
\begin{aligned}
m_{total} &= \begin{cases} 0.024 \times D^{2.500} + 0.059 \times D^{1.485} + 0.061 \times D^2 & (n \leq 32) \\ 0.002 \times D^{3.052} + 0.059 \times D^{1.485} + 0.061 \times D^2 & (n \geq 32) \end{cases} \\
D_{stowed} &= \begin{cases} 0.00922 \times D^{1.531} & (n \leq 32) \\ 0.00004 \times D^{2.633} & (n \geq 32) \end{cases} \\
H_{stowed} &= \begin{cases} 0.319 \times D^{0.910} & (n \leq 32) \\ 0.294 \times D^{0.926} & (n \geq 32). \end{cases}
\end{aligned}
\tag{2.16}
$$

2.5 Scaling of Natural Frequencies of Vibration

2.5.1 Finite Element Model and Boundary Conditions

A geometrically nonlinear, high-fidelity finite element model was developed in ABAQUS/CAE 2017 to analyze the natural frequencies of vibration for deployable mesh reflectors. The model incorporated all structural components, each individually represented, as described below.

The front and rear nets were modeled using truss elements (T3D2), where each edge of a triangular facet consisted of a single truss element. The perimeter truss members—longerons, battens, and diagonals—were modeled with 20 beam elements (B31). Pin joints, allowing relative rotation, were used to connect adjacent elements. The metallic mesh was represented as point masses distributed across the nodes of the front net. Additionally, the mass of the joints and deployment actuators was modeled as point masses connected to the joints of the perimeter truss. A PREDEFINED STRESS FIELD was assigned, corresponding to the prestress levels for each structural component, as determined in the optimization process in Section 2.2.2. Tension tie forces were applied to the inner nodes of both the front and rear nets. The model was set up in the operational geometric configuration of the reflector, with the prestress applied, ensuring minimal geometry changes during the geometrically nonlinear iteration to reach the prestressed equilibrium configuration.

The first step involved performing a static equilibrium analysis under the predefined stress field and tension tie forces. This provided the deformed geometry and stiffness of the reflector. A subsequent modal analysis was then carried out for the structure under the boundary conditions of interest and at equilibrium, to determine the natural frequencies and their corresponding mode shapes.

Two boundary conditions were considered. The first assumed that the reflector was attached to a massive spacecraft via a *prime batten*, designed to avoid interference with the perimeter truss deployment. This batten, shown in Fig. 2.15(a), was connected to the perimeter truss at three joints in the upper truss layer and one joint in the lower layer. In ABAQUS, this batten-supported boundary condition was implemented by restricting the six degrees of freedom (DoFs) at these four joints, as depicted in Fig. 2.15(b).

The second boundary condition assumed a free-free scenario, capturing the increasing dominance of the reflector's dynamics relative to the spacecraft as its size increases.

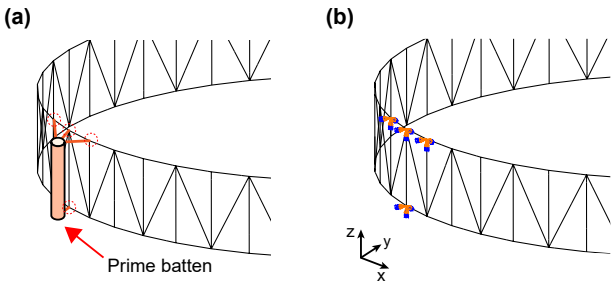

Figure 2.15: Batten-supported boundary condition: a) prime batten, and b) boundary conditions in finite element model.

2.5.2 Natural Frequencies and Mode Shapes

Key results from the finite element modal analysis for reflectors with $F/D = 1.0$ are presented in Fig. 2.16. The log-log trend for the lowest natural frequencies, shown in Fig. 2.16(a), forms a straight line with a negative slope, indicating that the frequencies follow a negative power law as the reflector diameter increases. Typical mode shapes are illustrated in Fig. 2.16(b) and Fig. 2.16(c), respectively, for the batten-supported and free-free boundary conditions.

For the batten-supported boundary condition, two dominant mode shapes emerge: a lateral mode, where the structure rotates around the prime batten, and a vertical mode, where the structure behaves as a cantilever, moving primarily in the z-direction as it vibrates up and down. The natural frequencies of these modes are rather close to each other, with the vertical mode being dominant for reflectors with $D < 25$ m, while the lateral mode becomes dominant for $D > 25$ m.

Under the free-free boundary condition, the fundamental mode exhibits a saddle-like shape, as depicted in Fig. 2.16(c). Notably, the fundamental frequency in the free-free case is significantly higher—about an order of magnitude—than in the batten-supported scenario.

The modal analysis results were fitted to power laws, as shown in Fig. 2.16(a), with RMS errors of 0.014, 0.003, and 0.116 Hz for the lateral, vertical, and saddle modes, respectively. The analytical expressions for the natural frequencies (in Hz) for $F/D = 1.0$ are as follows:

$$\begin{aligned} f_{lateral} &= 217.2 \times D^{-1.699} \\ f_{vertical} &= 88.43 \times D^{-1.419} \\ f_{saddle} &= 738.1 \times D^{-1.357}. \end{aligned} \tag{2.17}$$

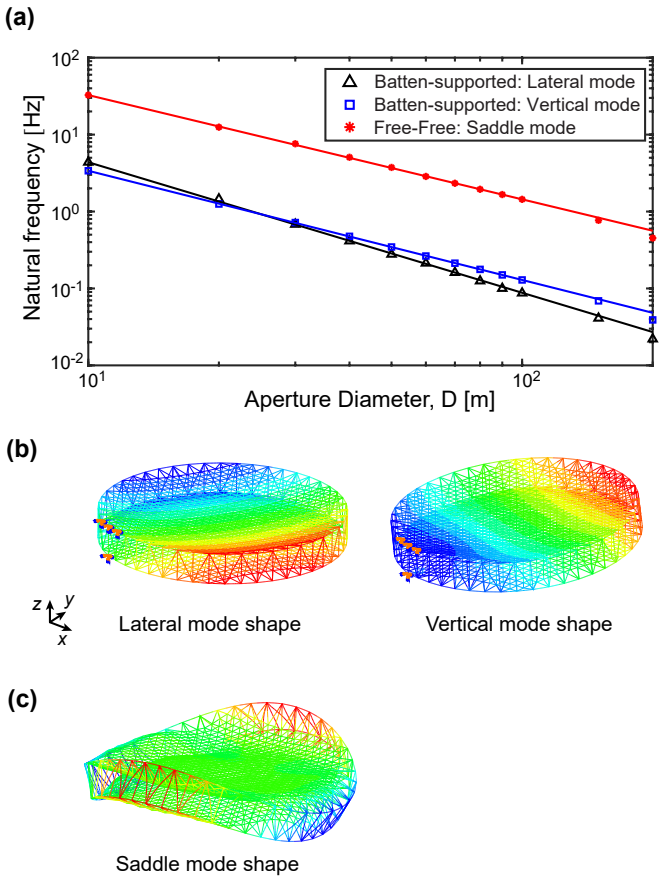

Figure 2.16: Natural frequencies and mode shapes for $F/D = 1.0$: a) frequency trends, b) first two mode shapes for prime-batten support condition, and c) first mode shape for free-free condition.

The prestressed modal analysis for mesh reflectors with $F/D = 0.5$ and $F/D = 0.7$ followed a similar procedure as the one used for $F/D = 1.0$. The corresponding scaling laws for natural frequencies were derived and are presented in Fig. 2.17.

For the batten-supported boundary condition, the first two natural frequencies correspond to the lateral and vertical modes, respectively. Unlike the $F/D = 1.0$ case, the lateral mode is the fundamental mode across all aperture diameters for both $F/D = 0.5$ and $F/D = 0.7$. Under the free-free boundary condition, the fundamental vibration mode is saddle-like, with frequencies significantly higher than those observed under batten-supported conditions.

In log-log space, all natural frequencies form straight lines with negative slopes, indicating a similar power-law relationship as for the case of $F/D = 1.0$ where the natural frequencies decrease as the reflector diameter increases. The results from

the modal analysis have been fitted to power laws as before, and the corresponding analytical expressions for reflectors with $F/D = 0.5$ is as follows:

$$\begin{aligned} f_{lateral} &= 218.1 \times D^{-1.839} \\ f_{vertical} &= 158.3 \times D^{-1.477} \\ f_{saddle} &= 1005 \times D^{-1.407}. \end{aligned} \tag{2.18}$$

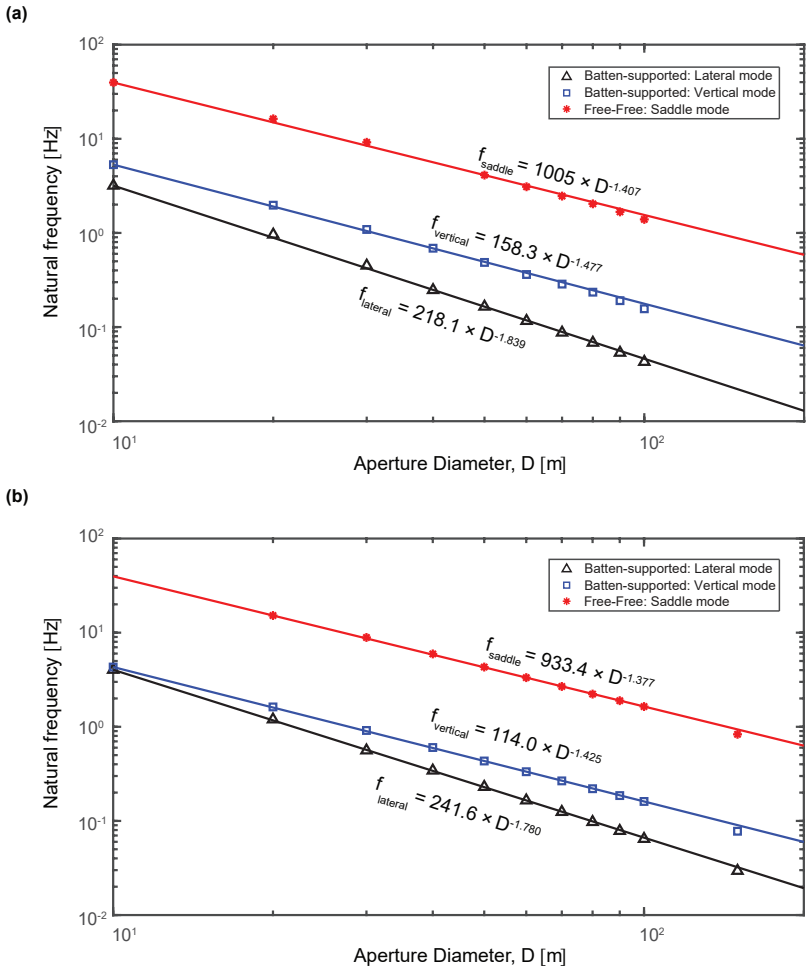

Figure 2.17: Natural frequency trends: a) $F/D = 0.5$, and b) $F/D = 0.7$.

For reflectors with $F/D = 0.7$, the analytical expressions are:

$$\begin{aligned} f_{lateral} &= 241.6 \times D^{-1.780} \\ f_{vertical} &= 114.0 \times D^{-1.425} \\ f_{saddle} &= 933.4 \times D^{-1.377}. \end{aligned} \tag{2.19}$$

2.5.3 Semi-Analytical Models for Fundamental Frequencies

While the high-fidelity modal analysis provides precise estimates of natural frequencies and mode shapes for reflectors of various apertures, the computational

demands become substantial for larger reflectors due to the increasing number of structural elements. For instance, the high-fidelity models for $D = 100$ m and $D = 200$ m contain approximately 15000 and 32000 structural elements, respectively. A semi-analytical model offers a faster yet accurate alternative for estimating these modal parameters.

Figure 2.18 illustrates the semi-analytical approach. The concept is to homogenize the mesh reflector to an edge-stiffened circular elastic plate. The cable nets are modeled by a flat continuum disk with equivalent stiffness, while the perimeter truss is represented as an equivalent hoop attached to the disk's outer edge. This approach can be applied to all mode shapes, though the model details vary. Here, the semi-analytical model for the lateral mode (the lowest frequency mode for larger apertures under batten-supported boundary condition) and the saddle mode are presented.

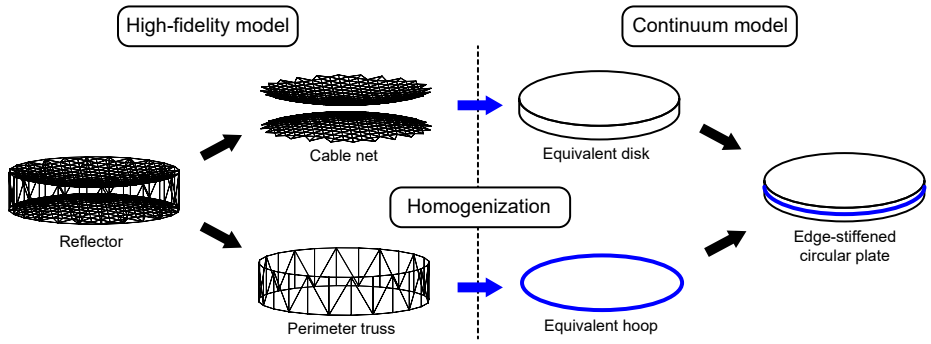

Figure 2.18: Semi-analytical modeling scheme.

For the batten-supported boundary condition, the lateral mode corresponds to an in-plane vibration where the reflector rotates about the three fixed joints in the perimeter truss that are constrained by the prime batten. This mode can be modeled as a 1-DoF mass-spring system, as shown in Fig. 2.19(a), where m_{eq} is the total mass, and I_{eq} is the moment of inertia of the reflector around a horizontal axis through its center of mass. The equivalent torsional stiffness, k_{eq}, of the torsional spring attached to the rigid bar of length $D/2$ is derived from an elastic analysis of the equivalent edge-stiffened continuum disk subjected to the same boundary conditions as the reflector, and loaded by an external couple, as shown. The three supports of the disk represent the constraints imposed by the prime batten on the upper ring of longerons.

Figure 2.19(b) illustrates the homogenization of the front net's stiffness. The rear net is not considered, as the lower ring of longerons is effectively free to rotate. The

truss elements of the front net are assumed to be coplanar, with a uniform tessellation of equilateral triangles, with edge length L. The equivalent homogenized stiffness matrix for a single-layer truss tessellation, A_{SL}, is calculated by superposition of three parallel trusses [4], Fig. 2.19(b), with modulus E_n and cross-sectional area A_n:

$$A_{SL} = \frac{3\sqrt{3}E_n A_n}{4L}. \tag{2.20}$$

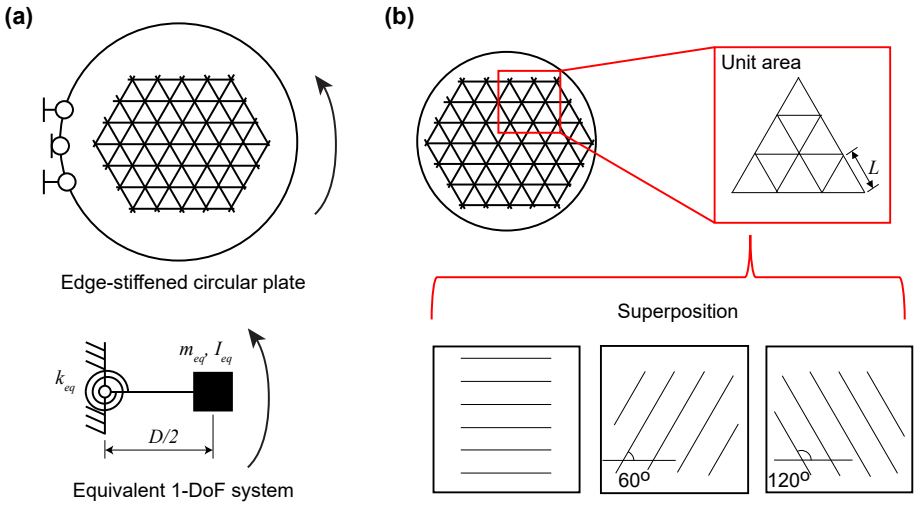

Figure 2.19: Semi-analytical model to estimate lateral mode: a) 1-DoF model, and b) homogenization of the net.

The equivalent continuum Young's modulus, E^*, and Poisson's ratio, ν^*, are (see Appendix A for details):

$$E^* = \frac{2\sqrt{3}E_n A_n}{3t_n L}, \quad \nu^* = \frac{1}{3}. \tag{2.21}$$

To complete the semi-analytical model of the edge-stiffened disk, a circular hoop, representing the longerons positioned along the perimeter of the front net and matching their cross-section, is attached to the disk's edge. As illustrated in Fig. 2.19(a), the equivalent torsional stiffness of the complete model, k_{eq}, is estimated by evaluating the rotation of this model under a given moment. The moment of inertia is the sum of I_{eq} and the parallel axis contribution, and the natural frequency is calculated from this system as follows:

$$f_{lateral} = 2\pi\sqrt{\frac{k_{eq}}{m_{eq}D^2/4 + I_{eq}}}. \tag{2.22}$$

Figure 2.20 compares the natural frequencies computed from the finite element analysis with those obtained from the semi-analytical approach. The results, also presented in Table 2.7, show that the lateral mode frequencies align well with the high-fidelity model, with errors reaching up to 22.27% for the largest diameters. This error is primarily due to differences between the actual cable net stiffness and the homogenized disk model. It is important to note, however, that Eq. 2.22 is applicable for all values of F/D, unlike the high-fidelity approach, which necessitates a separate model (and the associated computational costs) for each variation in F/D.

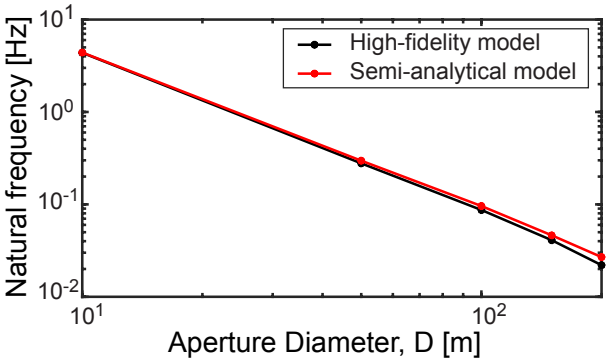

Figure 2.20: Natural frequency corresponding to lateral mode.

Table 2.7: Natural frequency of lateral mode (high-fidelity model vs. semi-analytical model)

	Natural frequency (Hz)		
D(m)	High-fidelity model	Semi-analytical model	Error (%)
10	4.346	4.371	0.58
50	0.276	0.294	6.54
100	0.086	0.095	10.30
150	0.041	0.046	12.39
200	0.022	0.027	22.27

As opposed to the lateral vibration mode, the saddle mode involves an out-of-plane motion under free-free boundary conditions, requiring the bending stiffness of the equivalent model to estimate k_{eq}. The semi-analytical model is therefore modified to estimate the bending stiffness of the prestressed nets and the perimeter truss's contribution. The bending and torsional stiffnesses of the continuum model are calculated by multiplying the in-plane continuum stiffness of each net by the square of the local distance between the nets [4].

This model can be further refined by accounting for the fact that the x, y plane projections of the triangles connecting the inner net to the perimeter truss are not equilateral. The in-plane stiffness of the central hexagonal region, composed of identical equilateral triangles, remains A_{SL} as before. The area between the perimeter truss and the central hexagon features a coarser cable pattern, as illustrated in Fig. 2.21(a). The equivalent material properties of the disk were derived by considering these distinct cable patterns, allowing for differences in angles and distances between the cables in the boundary region. The angle between the cables, β, is expressed as:

$$\beta = \tan^{-1}\left(\frac{L}{g}\right) = \tan^{-1}\left(\frac{4\left(2+\sqrt{3}\right)L}{D}\right). \tag{2.23}$$

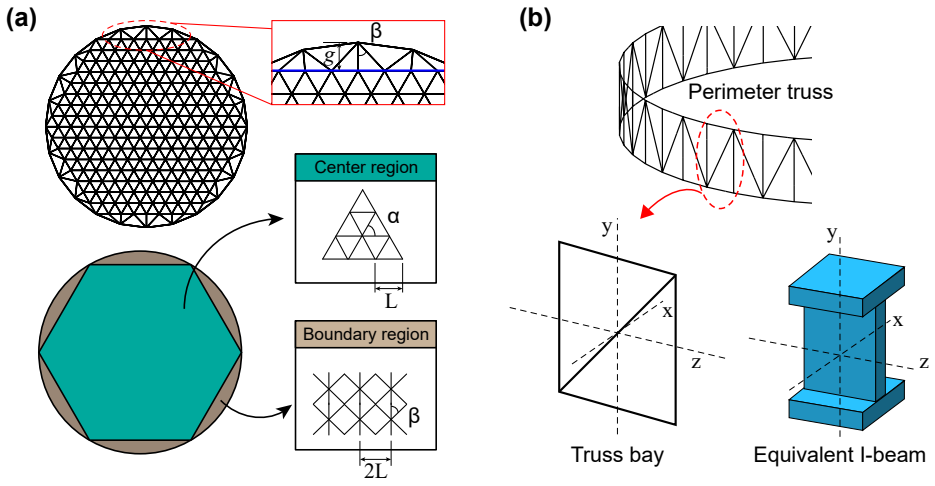

Figure 2.21: Semi-analytical model for free-free saddle mode: homogenization of a) net, and b) perimeter truss.

The ABD stiffness matrix for the equivalent disk was then obtained following the derivation for double-layer space frames outlined in [4]. Since the front and rear nets are identical, $A \approx 2A_{SL}$ and $D \approx A_{SL}(2z)^2$, where z is the distance between the two nets. Substituting Eq. 2.1 and using $r^2 = x^2 + y^2$, the ABD matrix at a radial distance r from the axis of the paraboloid is expressed as:

$$ABD\,(r) = \begin{bmatrix} A & B \\ B^T & D\,(r) \end{bmatrix} = \begin{bmatrix} 2A_{SL} & 0 \\ 0 & \left(2s_0 + \frac{r^2}{2F}\right) A_{SL} \end{bmatrix} \tag{2.24}$$

where the B matrix is zero, for symmetry.

The perimeter truss consists of identical bays, as shown in Fig. 2.21(b). In the proposed semi-analytical model for the saddle vibration mode, the perimeter truss was homogenized to an equivalent I-beam, having the same second moment of area as a bay for all axes. This equivalent hoop was again attached to the edge of the equivalent disk, and a modal analysis was performed on the continuum model using ABAQUS/CAE 2017.

Figure 2.22(a) compares the saddle mode frequencies obtained from the high-fidelity simulations with those from the semi-analytical model. The mode shape produced by the semi-analytical approach shows good qualitative agreement, as illustrated in Fig. 2.22(b), and the corresponding numerical values are provided in Table 2.8.

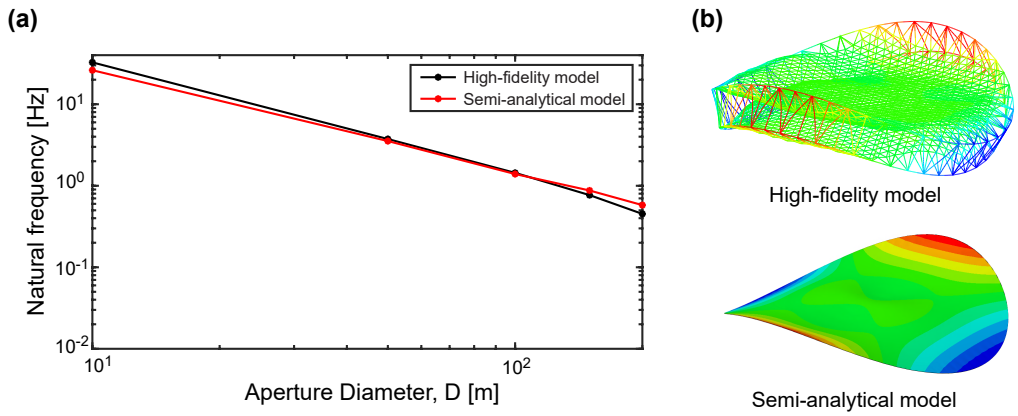

Figure 2.22: Natural frequency of free-free saddle mode: a) frequency comparison, and b) mode shape comparison.

Table 2.8: Natural frequency of saddle mode (high-fidelity model vs. semi-analytical model)

	Natural frequency (Hz)		
D(m)	High-fidelity model	Semi-analytical model	Error (%)
10	32.473	26.153	19.85
50	3.702	3.535	5.56
100	1.430	1.393	3.26
150	0.764	0.875	13.93
200	0.452	0.579	28.10

2.6 Chapter Conclusions

This chapter has presented the design and analysis of deployable mesh reflectors, spanning aperture sizes from 10 to 200 meters. The reflector geometry is tailored to

meet the stringent surface accuracy requirement of 0.6 mm, necessary for operation at a 10 GHz RF frequency. Through a comprehensive investigation of the reflector's kinematic and static properties, it was determined that a design composed entirely of triangular facets—without cross-wires—ensures both kinematic and static determinacy. This approach guarantees a unique shape and unique equilibrium solution under prestress. The prestress distribution across the structural elements is optimized by adjusting the tension tie forces applied to the net. Across all aperture sizes, the optimized designs exhibit a lower standard deviation in cable tension and reduced compressive forces on the perimeter truss compared to non-optimized designs.

The structural design methodology has been detailed, with mass and volume analyzed at the component level. For optimized designs, the areal density remains nearly constant as the reflector diameter increases, while non-optimized designs display a rising areal density with increasing size. Scaling laws for mass and volume are derived as functions of aperture diameter. The study concludes that the designed reflectors are feasible for launch with diameters up to approximately 70-100 meters using commercially available launch vehicles. More importantly, the findings emphasize that stowed volume, rather than mass, poses the primary constraint on the launch envelope, underscoring the necessity for innovative design approaches for ultra-large space structures.

Additionally, the natural frequencies of the reflector have been examined under two boundary conditions: batten-supported and free-free. Scaling laws for the fundamental frequencies are proposed based on high-fidelity simulations. A semi-analytical model has been developed for both boundary conditions, utilizing a homogenization technique that approximates the net and perimeter truss as equivalent continua. The semi-analytical model's predictions closely align with high-fidelity simulations while offering a substantial reduction in computational time (from about 48 hours to just a few minutes), with its validity extending to all F/D ratios.

This study has achieved its overall aim of providing practical insights into the design and scaling of deployable mesh reflectors, evaluating existing design approaches, and advancing the understanding of key metrics for assessing these structures for future applications. Moreover, this study has extended key metric data beyond the 25 m aperture presented in previous studies, thereby establishing a baseline for comparing large deployable mesh reflectors with ISA concepts, as discussed in Chapter 3.